

Magnetic Resonance Characterization of Stem Cell Based Tissue - Engineered Cartilage  
and Bone

BY

PADMABHARATHI POTHIRAJAN

B.E., Anna University, India, 2008

THESIS

Submitted as partial fulfillment of the requirements  
for the degree of Master of Science in Bioengineering  
in the Graduate College of the  
University of Illinois at Chicago, 2014  
Chicago, Illinois

Defense committee:

Dr. Richard L. Magin, Chair

Dr. Mrignayani Kotecha, Advisor

Dr. Anne George, Department of Oral Biology

*I would like to dedicate this thesis to my spouse and family.*

*Thank you for all the love and encouragement, all the best things about me are because of you.*

## ACKNOWLEDGEMENTS

First and foremost, I would like to thank my advisor Dr. Mrignayani Kotecha, for all the support and guidance throughout my work. She provided me guidance in all areas that helped me accomplish my research goals and enjoy myself in the process. I would like to thank my thesis committee, Dr. Richard Magin and Dr. Anne George for their unwavering support and assistance.

I would like to thank Dr. Sriram Ravindran and Dr. Syam P. Nukavarapu who have supported in my research. I wish to thank Dr. Robert Kleps, Director of RRC facility who provided me the training in MRI and NMR experiments and also helped me in my experiments. I thank Dr. Boris Epel for providing Matlab program for MRI data processing. A special thanks to all my lab mates and Ziyang Yin for their invaluable assistance, training and suggestions that contributed to the study.

Finally I would like to express my heartfelt gratitude to my family and friends who have loved and supported me throughout this process. Without their support, I would never have made it so far.

## TABLE OF CONTENTS

<u>CHAPTER</u>	<u>PAGE</u>
1. INTRODUCTION.....	1
2. THEORY .....	3
2.1 Tissue Engineering.....	3
2.1.1 Cells .....	4
2.1.2 Biomaterials/ Scaffold .....	6
2.1.3 Growth Factors.....	7
2.2 Cartilage Tissue Engineering .....	8
2.3 Bone Tissue Engineering.....	9
2.4 Osteochondral Tissue Engineering.....	10
2.5 Magnetic Resonance Imaging (MRI).....	12
2.5.1 Principles of MRI.....	13
2.5.2 MRI Hardware .....	22
2.5.3 Sodium MRI .....	24
3. MRI CHARACTERIZATION OF OSTEOGENIC AND CHONDROGENIC TISSUE CONSTRUCT .....	25
3.1 Materials and Methods .....	25
3.1.1 Sample Preparation.....	25
3.1.2 Biochemical analysis.....	26
3.1.3 Proton MRI measurements .....	27
3.1.4 Sodium MRI measurements .....	29
3.2 Results and Discussions .....	29
3.2.1 Proton MRI experiment.....	29
3.2.2 Sodium MRI experiment.....	32
3.2 Conclusions .....	34

## TABLE OF CONTENTS (continued)

<u>CHAPTER</u>	<u>PAGE</u>
4. MRI CHARACTERIZATION OF POLYMER - HYDROGEL SCAFFOLD, ECM, CELLS	35
4.1 Materials and Methods .....	36
4.1.1 Sample Preparation .....	36
4.1.2 Biochemical analysis .....	38
4.1.3 Proton MRI measurements .....	38
4.2 Results and Discussions .....	39
4.3 Conclusions .....	41
5. CONCLUSIONS AND FUTURE WORK .....	42
6. REFERENCES .....	43
7. VITA .....	50

## LIST OF TABLES

<u>TABLE</u>	<u>PAGE</u>
1. Some common natural and synthetic polymers used in tissue engineering.....	7
2. Rules for determining the net spin of a nucleus .....	13
3. Calculated mean and standard deviation of proton MRI parameters in control gel, osteogenic and chondrogenic constructs .....	32
4. Calculated average sodium concentration for osteogenic and chondrogenic constructs using sodium MRI.....	33
5. Measured and calculated T2 for the scaffold system with and without cells, T2 for ECM growth only and T2 for cells at day 7,19 and 26.....	40
6. Measured T1 and ADC for the scaffold system with and without cells at day 7,19 and 26 .....	41

## LIST OF FIGURES

<u>FIGURE</u>	<u>PAGE</u>
1. Basic building blocks of tissue engineering.....	4
2. Stem cell differentiation diagram.....	5
3. Schematic diagram of native cartilage tissue and engineered cartilage tissue.....	9
4. Osteochondral structure showing different zones of cartilage, bone and their interface	11
5. Magnetic moment vectors pointing (a) in random directions in the absence of external magnetic field (b) aligned in the presence of external magnetic field .....	14
6. Spin-echo pulse sequence timing diagram .....	18
7. Inversion recovery pulse sequence timing diagram.....	19
8. CPMG pulse sequence timing diagram.....	20
9. Multi slice multi echo pulse sequence timing diagram .....	21
10. Diffusion weighted spin-echo pulse sequence timing diagram .....	22
11. Schematic diagram of MRI scanner and components .....	23
12. Schematic of chondrogenic and osteogenic construct preparation.....	26
13. Confocal images of osteogenic and chondrogenic constructs stained for different ECM proteins .....	27
14. (a) Bruker 500 MHz (11.7 T) micro-imaging facility, (b) Proton and proton/ sodium double tuned 5mm RF coil .....	28
15. Axial slices from T2 weighted MRI images of osteogenic construct (left) and chondrogenic construct (right) .....	29

LIST OF FIGURES (continued)

<u>FIGURE</u>	<u>PAGE</u>
16. T1, T2 and ADC maps of chondrogenic construct, osteogenic construct and control gel in Fluorinert oil .....	31
17. Image obtained from sodium MRI experiment at 11.7 T (left – osteogenic construct and right – chondrogenic construct).....	33
18. Schematic diagram of “Polymer-Hydrogel” scaffold fabrication.....	37
19. Immunofluorescence staining of “Polymer Hydrogel “scaffold showing chondrogenesis of stem cells .....	38
20. T2 maps for (A) scaffold (B) engineered cartilage (scaffold + cells + ECM) at day 7 (C) engineered cartilage at day 26 (D) engineered cartilage-without-cells (ECM + scaffold) at day 7 (E) engineered cartilage-without-cells at day 26 .....	40

## LIST OF ABBREVIATIONS

ADC	Apparent diffusion coefficient
ALP	Alkaline phosphatase
BM-hMSCs	Bone marrow derived human mesenchymal stem cells
BMPs	Bone morphogenic proteins
CPMG	Carr-Purcell-Meiboom-Gill pulse sequence
ECM	Extra cellular matrix
EGFs	Epidermal growth factors
FGFs	Fibroblast growth factors
FID	Free induction decay
FT	Fourier transforms
GAG	Glycosaminoglycan
GEFC	Gradient echo with flow compensation
HBSS	Hank's Balanced Salt Solution
HMSCs	Human marrow stromal cells
IGFs	Insulin like growth factors
IR	Inversion recovery
MRS	Magnetic resonance spectroscopy
MRI	Magnetic resonance imaging
MSC	Mesenchymal stem cell
MSME	Multi slice multi echo Sequence
PEG	Poly (ethylene glycol)

## LIST OF ABBREVIATIONS (continued)

PG	Proteoglycans
PGA	Poly (glycolic acid)
PGFs	Platelet derived growth factors
PHA	Polyhydroxyalkanoate
PLGA	Copolymer poly (lactic-co-glycolic acid)
PLLA	Poly (L-lactic acid)
RAREVTR	RARE with variable TR
ROI	Region of interest
RF	Radio frequency
SE	Spin Echo
TE	Echo time
TGF- $\beta$	Transforming growth factors
TR	Repetition time

## 1. INTRODUCTION

Musculoskeletal disorders are the major cause of disability and discomfort among adults in the United States [1]. Osteoarthritis, trauma, developmental issues, sports injuries, and motor accidents commonly cause cartilage and its underlying subchondral bone damage. Currently, there are no effective treatment such as autologous chondrocyte implantation, osteochondral autograft transfer system and marrow stimulation as they don't have the potential to regenerate the native like cartilage [2-5]. Therefore, cartilage, bone or osteochondral tissue engineering are expected to provide a solution by offering functional native-like cartilage, bone or osteochondral interfaces. One of the major issues in translating major breakthroughs of tissue engineering to clinics is the lack of adequate non-invasive characterization procedures at all stages of tissue growth, from cell seeding to post-implantation. Magnetic resonance spectroscopy (MRS) and imaging (MRI) are leading non-invasive characterization techniques for engineered cartilage and bone tissues [6-10]. The major advantage of MR techniques is in their easy translation to clinics. Much of the current efforts in MR characterization of engineered tissues are focused on a single tissue type, however, in particular region such as osteochondral interfaces, the comparative MR properties of cartilage and bone tissues is of utmost interest.

In the first study, as a first step to characterize osteochondral tissues, we established an MRI characterization protocol for tissue-engineered bone and tissue-engineered cartilage. For this study, osteogenic and chondrogenic tissue constructs

were developed by seeding HMSCs (2 million/ml) in collagen/chitosan gel at the ratio of 1:1 and differentiated with osteogenic and chondrogenic growth media. We compared proton and sodium MRI properties of these tissue constructs and the control collagen/chitosan gel at 11.7 T ( $^1\text{H}$  freq. = 500 MHz) microimaging MRI system. We found that, the development of bone and cartilage was clearly distinguishable using both proton and sodium MRI.

In second study, we present preliminary MRI data for chondrogenic differentiation of human bone marrow derived stem cells seeded onto the specially designed “polymer-hydrogel” osteochondral matrices to separate out various contributions in water MR parameters. The scaffold system used in this study is uniquely designed to best support osteochondral defect repair and regeneration. The proton  $T_1$ ,  $T_2$  and diffusion MRI experiments were performed on these chondrogenic scaffolds for scaffold only, tissue-engineered cartilage (scaffold with cells and ECM), and fixed tissue-engineered cartilage using a 11.7 T ( $^1\text{H}$  freq. = 500 MHz) microimaging MRI system. Though the contribution of scaffold in MR parameter is found to be the most dominate, we made an attempt to identify the contribution of ECM and cells in water  $T_2$  relaxation time.

## 2. THEORY

### 2.1 Tissue Engineering

Tissue engineering is an emerging multidisciplinary field involving engineering, medicine and biology to replace damaged tissue or organs to promote the health and quality of life for patients worldwide. It uses a combination of cells, biocompatible scaffolds, and suitable signaling molecules to improve or replace biological functions. In the early stage of tissue engineering, readily available biocompatible materials were used that had potential for growth. However currently, advanced complex tissue engineered materials strategies are being employed that have potential to replace the native tissue using the natural mechanisms for repair, remodeling and regeneration [11]. The central paradigm underlying tissue engineering is the creation of neotissue, which is achieved by seeding cells onto a bioadsorbable scaffold matrix with incorporated growth factors [12]. This matrix acts as a three-dimensional scaffold until proliferating cells produce sufficient ECM, which is followed by scaffold degradation, neotissue formation, and growth. The basic building blocks of tissue engineering are illustrated in Figure 1 and explained in following sections.

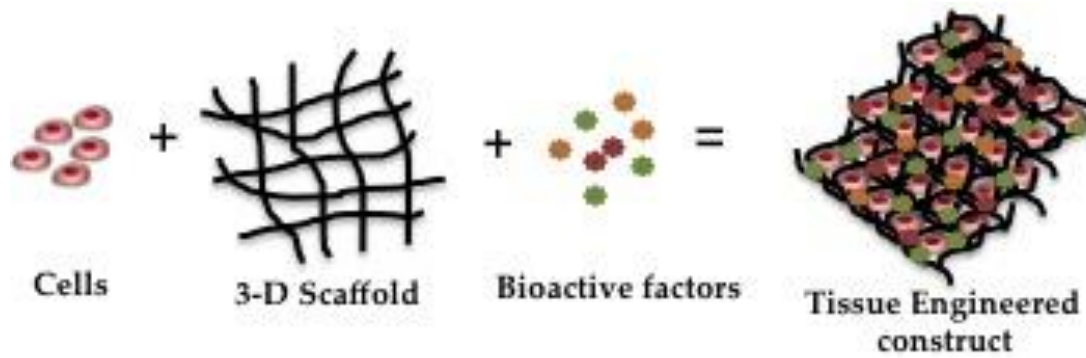


Figure 1: Basic building blocks of tissue engineering. This figure is inspired by [13].

### 2.1.1. Cells

Cells are the most basic functional and structural units of tissues and organs. Tissue engineering uses either autologous cells (stem cells from same person) or stem cells from other donor. Stem cells are derived from different sources like embryonic tissues, fetal tissues, cord blood and adult tissues (different kind throughout the body). Based on their origin these stem cells possess varying capacity to multiply and differentiate. The fertilized egg, Zygote, is referred as totipotent as it has the highest degree of plasticity. After fertilization, zygote begins to divide and form a blastocyst. Cells derived from the blastocyst of embryo are called embryonic stem cells. They have the capability of dividing into endodermal cells, ectodermal cells and mesodermal cells. These cells are also called 'pluripotent' stem cells as they have the potential to become more than 200 types of cells in the body. After 8 weeks, embryo referred as fetus and these fetal stem cells as designed as "multipotent", as they are more tissue specific [14]. A more advanced stage of development is the adult stem cells, and they can be found in

blood, bone marrow, cornea, brain, skin, liver, skeletal muscle, gastrointestinal tract, dental pulp of teeth and pancreas [15]. Figure 2 illustrates the differentiation of stem cells from zygote to adult tissue specific stem cells.

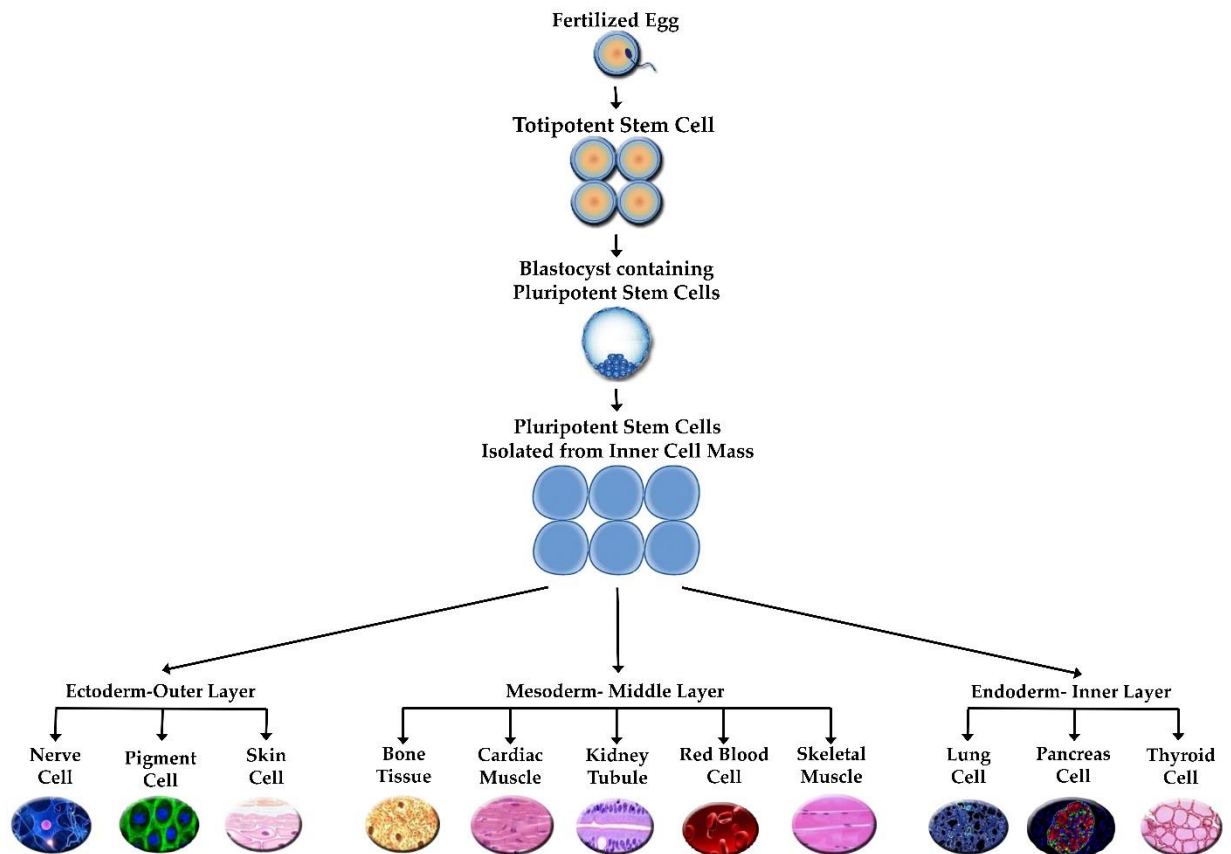


Figure 2: Stem cell differentiation diagram. This figure is inspired by [14].

### 2.1.2. Biomaterials/ Scaffold

When a tissue is severely damaged, it will cause damage to a large number of functional cells and also tissue matrix that is called extracellular matrix (ECM). Small molecule drugs or recombinant proteins do not have the potential to restore this loss. Therefore, for creating a neotissue, we need to provide an artificial or biologically derived ECM for cells. In tissue engineering, scaffolds act as a substitute for native ECM. The scaffold provides a three-dimensional (3-D) structure for the proliferation of cells into the targeted tissue. The important function of scaffold is to create an environment that enables 3-D cell growth and neotissue formation for providing a structure for organizing dissociated cells into an appropriate tissue [19]. There are two types of biomaterials/polymers utilized for scaffold fabrication: natural and synthetic. These biomaterials are selected based on their biocompatibility, mechanical property and bioadsorbability. Mostly, natural biodegradable polymers have been explored as they have the advantage of potential for offering more biocompatible template on which cells grow [16]. Table 1 lists some commonly used polymers in tissue engineering applications.

Natural Biomaterial	Synthetic Biomaterial
Collagen	Poly (glycolic acid) [PGA]
Chitosan	Poly (L-lactic acid)[PLLA]
Fibrin	Copolymer poly (lactic-co-glycolic acid)[PLGA]
Elastin	Poly (ethylene glycol)[PEG]
Glycosaminoglycan [GAG]	Polyhydroxyalkanoate [PHA]

Table 1: Some common natural and synthetic polymers used in tissue engineering [11].

### 2.1.3. Growth factor

Regulatory biomolecules (growth factors) and cytokines are released by different sorts of cells in a diverse manner to carry out a specific reaction. The factors that are associated with cells involved in the immune system are referred as cytokine, but in many instances it is used as a synonym for cytokines. Depending upon the tissue and the site where the regeneration is expected, different growth factors are used. Here are commonly used growth factors in tissue engineering: epidermal growth factors (EGFs), fibroblast growth factors (FGFs), platelet derived growth factors (PGFs), insulin like growth factors (IGFs), transforming growth factors (TGF-B), and bone morphogenic proteins (BMPs) [17].

## 2.2 Cartilage Tissue Engineering

Currently, the diseased or damaged cartilage tissue is treated using marrow stimulation, autologous chondrocyte implantation and osteochondral autograft transfer system [9, 18]. However these treatment options are inadequate for long-term restoration of cartilage function. Tissue engineered cartilage is expected as a potential alternate to regenerate the biomechanical and functional properties of native like cartilage. The main components of cartilage tissue are chondrocyte cells and ECM. The cartilage ECM is made up of tissue water, type II collagen, proteoglycans, glycoproteins and non- collagenous proteins. The engineered cartilage also has the components of native articular cartilage but with a higher quantity of stem cells, chondrocytes, along with a high amount of proteoglycans than collagen and random/short collagen, type II fibrils. Figure 3 highlights few key differences between native articular cartilage and engineered cartilage derived from stem cells and scaffold based tissue engineering [9].

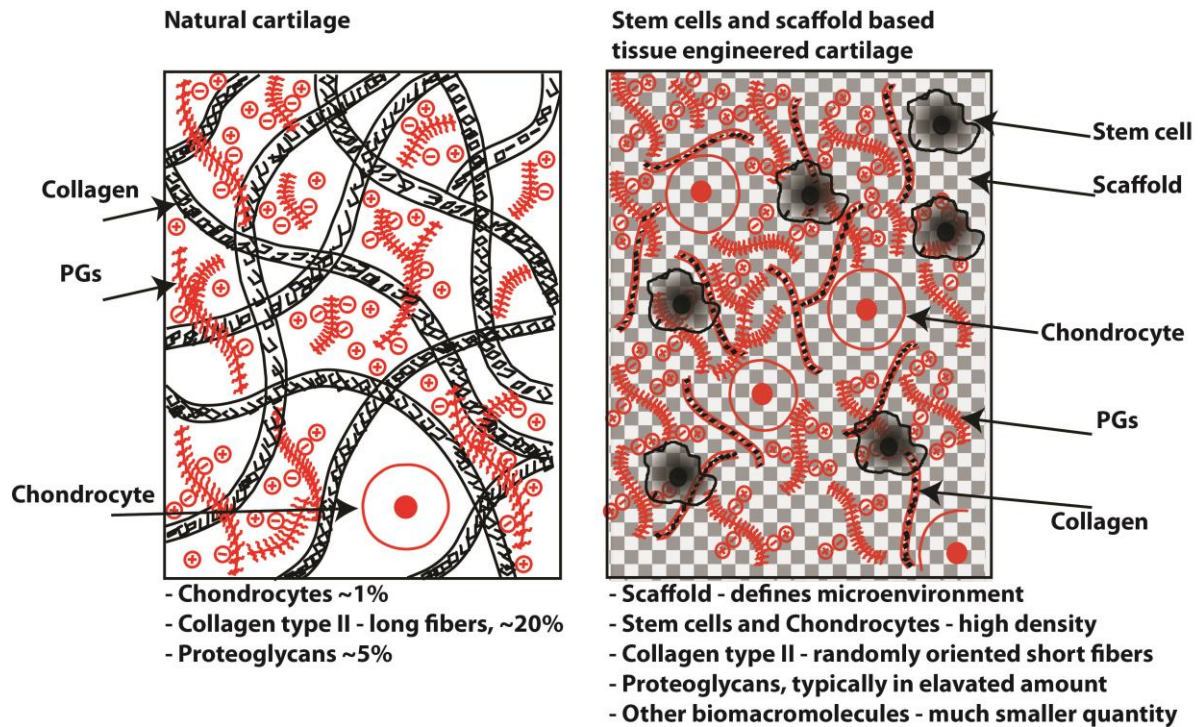


Figure 3: Schematic diagram of native articular cartilage tissue and engineered cartilage tissue [20]

### 2.3 Bone Tissue Engineering

Tissue engineered bone has been viewed as a potential method to replace the conventional use of bone grafts, bone bracing and many more methods used to treat bone damages. Bone is developed by two distinct processes: Intramembranous ossification and Endochondral ossification. Intramembranous ossification is a process in which mesenchymal stem cells (MSC) are differentiated into osteoblasts and directly form bone. Endochondral ossification is another process, which involves the formation of primitive cartilaginous tissue, which then undergoes calcification resulting in the formation of new bone by mesenchymal stem cells. [18]

The cells that are responsible for synthesis and mineralization of bone during

bone formation are osteoblasts. They are formed by the differentiation of osteogenic cells or osteogenic differentiation of mesenchymal stem cells. During cellular differentiation, osteoblasts produce many cell products including the essential enzyme alkaline phosphatase, hormones such as osteocalcin and collagen, type I. Alkaline phosphatase (ALP) converts organic phosphate to inorganic phosphate, resulting in the formation of calcium phosphate crystals which get deposited on the newly synthesized ECM that provides further cues for mineralization.

#### 2.4 Osteochondral Tissue Engineering

Osteochondral tissue engineering is a developing strategy that combines both cartilage and bone tissue engineering fundamentals for the regeneration of cartilage, bone and cartilage-bone interface. Cartilage can be distinguished into four different zones as shown in Figure 4. The outermost layer is the superficial zone, which is composed of 10-20% of the cartilage. The next layer is the middle zone, which comprises the most part of cartilage around 40-60%, and the last layer is deep and calcified cartilage zone, which is comprised of remaining thickness [21].

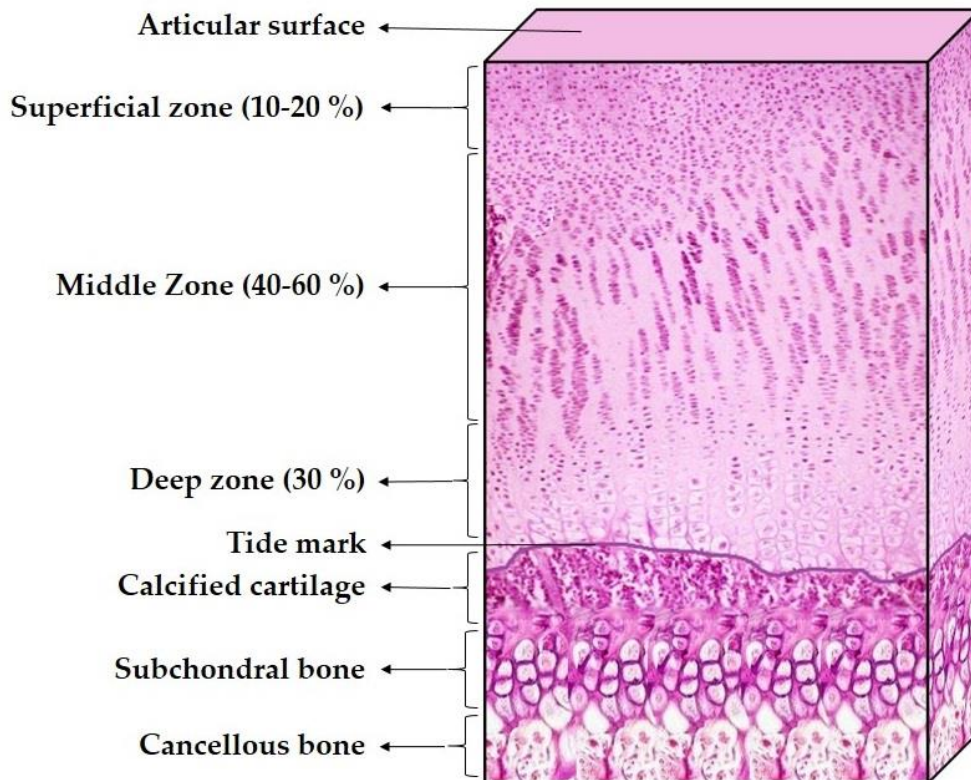


Figure 4: Osteochondral structure showing different zones of cartilage, bone and their interface. The figure is inspired by [53]

Each of these zones is defined by unique composition of cells and different proportions of ECM components. The superficial zone has a low amount of proteoglycan, densely packed cells and collagen fibrils that are parallel to the articular surface [22-25]. Middle zone is rich in proteoglycan and has less number of cells and obliquely oriented collagen fibrils [26,27]. The deep zone contains even smaller amount of proteoglycans compared with the middle zone and here, the cells and collagen fibrils are perpendicularly oriented to the articular surface [25]. Below the deep zone, there is a thin layer called “tide mark” that marks the transition from the deep zone to the

calcified zone. This zone has a smallest amount of collagen fibrils when compared with the deep zone that traverse through this tidemark layer [28]. Subchondral bone is the innermost region of the osteochondral structure and is composed of bony lamella and the trabeculae. This area provides most of the mechanical support to the joint. Underneath the subchondral bone is a region called cancellous bone with a solid mass of bone [29]. Because of the difference in the mechanical properties and biological composition of cartilage and bone, this interface is a complex tissue. Hence the design and fabrication of engineered osteochondral construct is a challenging task for the tissue engineers.

## 2.5 Magnetic Resonance Imaging (MRI)

Magnetic resonance imaging (MRI) is one of the most powerful and complex analytical techniques used worldwide in many different fields. MRI is a non-destructive technique with resolution of tens of microns and is used to produce high quality images of a given sample [30]. MRI relies on the magnetic properties of the atomic nucleus. When nuclei are placed in a strong magnetic field, nuclei resonate at a particular frequency in the radio frequency (RF) range of the electromagnetic spectrum. An important feature of MRI is that the excitation is done by RF pulses that are low energy non ionizing radiations [31]. Therefore, MRI is considered safe when compared to X-ray when applied to humans in clinical settings. As MRI is a

noninvasive technique; it can generate 2- dimensional and 3-dimensional images without slicing or dicing the sample [32].

### 2.5.1. Principles of MRI

#### a) Nuclear spin and magnetic moment.

Nuclei with odd number of protons and neutrons exhibit a special property called nuclear spin. All the atoms have atomic and mass number, from which we can calculate the nuclear spin, I.

Mass Number (No. of proton + No. of Neutron)	Atomic Number (No. of proton)	Nuclear Spin (I)
Even	Even	0
Odd	Even or odd	$\frac{1}{2}, \frac{3}{2}, \frac{5}{2} \dots$
Even	Odd	1,2,3....

Table 2: Rules for determining the net spin of a nucleus [34].

According to quantum mechanics, a nucleus whose nuclear spin is I, will have  $2I + 1$  possible orientations when placed in an external magnetic field. Normally, in the absence of a magnetic field, nuclei will be randomly oriented with equal energy. However, when these nuclei are placed in an external magnetic field ( $B_0$ ), the energy levels split and their directions will be aligned in the direction of external magnetic field or oppose the external magnetic field as shown in Figure 5. The difference in energy  $\Delta E$  between the two levels is proportional to the strength of the external

magnetic field strength.

$$\Delta E = h\nu_0 = h\gamma B_0/2\pi$$

Where  $h$  is Planck's constant,  $\nu_0$  is resonant frequency and  $\gamma$  is the gyromagnetic ratio.

Proton  $^1\text{H}$  is the most abundant (99.9%) naturally occurring nucleus with a non-zero spin and hence  $^1\text{H}$  – MRI is frequently used in measurements [48]. Water is the most abundant substance in human body, therefore, water proton MRI is a common diagnostic tool used in clinics. There are other biologically relevant nuclei like sodium ( $^{23}\text{Na}$ ), carbon ( $^{13}\text{C}$ ), oxygen ( $^{17}\text{O}$ ), nitrogen ( $^{15}\text{N}$ ), phosphorus ( $^{31}\text{P}$ ) etc., that possess nuclear spins and hence can be observed using MRI.

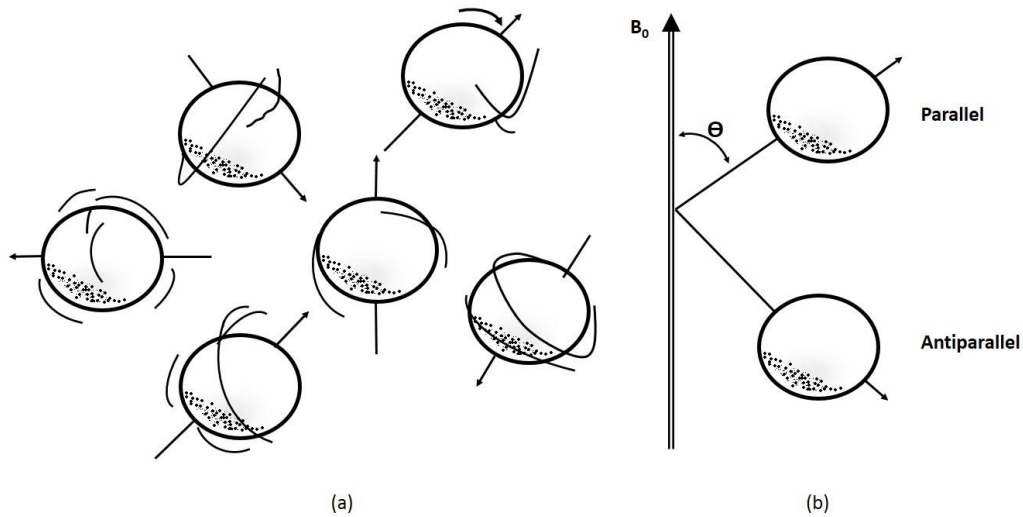


Figure 5: Magnetic moment vectors pointing (a) in random directions in the absence of external magnetic field b) aligned in the presence of external magnetic field. The figure is inspired by [32].

b) Larmor Frequency

When an external magnetic field is applied to the system, the nuclei precess around ( $B_0$ ). The frequency of precession is proportional to the strength of the magnetic field and is as termed the Larmor frequency ( $\omega_0$ ). The Larmor frequency is equivalent to the resonant frequency that cause the transition between the two energy levels of the spin and it is given by the following equation:

$$\omega_0 = \gamma B_0$$

c) Encoding

Normally, in any system image is obtained by two steps. First, spatial information is encoded into a measurable signal and then, encoded signal is decoded to produce an image. In MRI, the spatial encoding process is accomplished by acquiring NMR signal. Encoding comprises of slice selection and spatial encoding within the slice.

- Slice selection is achieved by applying a slice-selective RF excitation pulse that excites the spins in the chosen particular slice.
- Spatial encoding within the slice is then done by the application of frequency encoding and phase encoding gradients which allow the encoding of spatial location.
- The frequency encoding gradient encode signals into different frequencies, depending upon the spatial information toward the gradient

- The phase encoding gradient encodes the spatial signal location by different spin phases. The number of phase encoding gradients is directly related to the spatial resolution.
- K space is defined as the space covered by the frequency encoding and phase encoding data. Hence the number of points in the k-space is dictated by the number of frequency encoding steps and phase encoding steps indicated in the pulse sequence. Once all the k space has been assembled, Fourier transform (FT) is applied to reconstruct the image.

#### d) Relaxation processes

When RF signal is applied, the nuclei that have been aligned along the magnetic field are excited from lower to higher energy state. Once the excitation pulse has been turned off, these nuclei then return back to their lower energy equilibrium state. This process is known as relaxation. There are two mechanisms of relaxation for nuclear spins: Spin - lattice (longitudinal) relaxation and Spin - spin (transverse) relaxation.

##### i. Spin - lattice relaxation ( $T_1$ )

Equilibrium magnetization  $M_0$  is the net magnetization vector along the direction of the applied magnetic field  $B_0$  at equilibrium condition. When RF pulse is applied, it turns away magnetization from z to xy direction. When the RF pulse is terminated, nuclei in the higher energy state will lose their excess energy to

surrounding environment (or lattice). The time taken by the nuclei to return back to its equilibrium state is called the spin lattice relaxation time ( $T_1$ ). The Longitudinal magnetization,  $M_z$  is given by following equation,

$$M_z = M_0 (1 - e^{-t/T_1})$$

ii. Spin - spin relaxation ( $T_2$ )

The net magnetization which is placed in the XY plane will rotate about their Z axis and starts to dephase after the  $90^\circ$  pulse. The time constant, which describes the rate of decay of transverse magnetization,  $M_{XY}$  to its equilibrium state, is called the spin-spin relaxation time,  $T_2$ . In biological samples, usually, the recovery of magnetization in the Z-axis occurs slower than the decay of the magnetization from the transverse plane. Consequently,  $T_2$  is always less than or equal to  $T_1$  [33].

$$M_{XY} = M_{XY_0} e^{-t/T_2}$$

e) Pulse sequence

A pulse sequence is a series of defined RF pulse and magnetic field gradient pulse arranged in a time sequence to control NMR signal reception. Fourier transform is a mathematical operation, which converts these signals from the time domain to the frequency domain as the NMR Spectrum. There are two most important time parameters in the pulse sequence: Repetition time (TR- Time between consecutive  $90^\circ$

RF pulse) and the echo time (TE - Time between the application of 90° RF pulse and the echo). There are an infinite number of possibilities of pulse sequences. NMR signal, free induction decay (FID) is the primary transient signal in MRI. When RF pulse is turned off, magnetization  $M$  in the  $xy$  plane precess about  $z$  and this oscillating signal, decays as a function of time. This process is called FID.

i. Spin Echo

The spin echo sequence is the most commonly used pulse sequence in MRI experiments. In this sequence, a 90° RF pulse is applied to the system, which rotates the magnetization down to  $XY$  plane. This is followed by a 180° refocusing pulse, which causes the magnetization to recover and form an echo as shown in Figure 6. By varying TR and TE in the sequences, we can get  $T_1$ -weighted image (short TR and short TE), Proton or spin density (a long TR and short TE {first echo}), or  $T_2$ -weighted images (a long TR and long TE {second echo}).

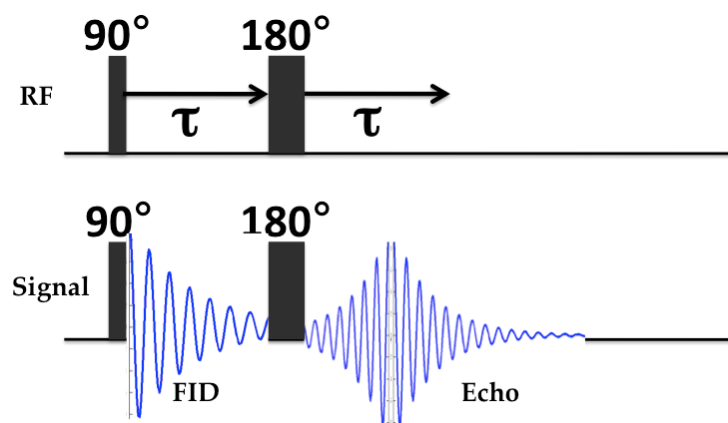


Figure 6: Spin echo pulse sequence timing diagram [35].

ii. Inversion Recovery (IR)

IR pulse sequence is a commonly used pulse sequence for  $T_1$  measurement. In this pulse sequence, a  $180^\circ$  inverting pulse is first applied. This rotates the net magnetization  $M_z$ , through  $180^\circ$ . The magnetization undergoes  $T_1$  relaxation and relaxes back to  $B_0$ . A  $90^\circ$  RF pulse is applied before it reaches an equilibrium (Figure 7). The time interval between the starting  $180^\circ$  pulse and the following  $90^\circ$  pulse is known as Inversion time. This  $90^\circ$  RF pulse brings the remaining longitudinal magnetization into the transverse plane where it can be detected by the RF coil.

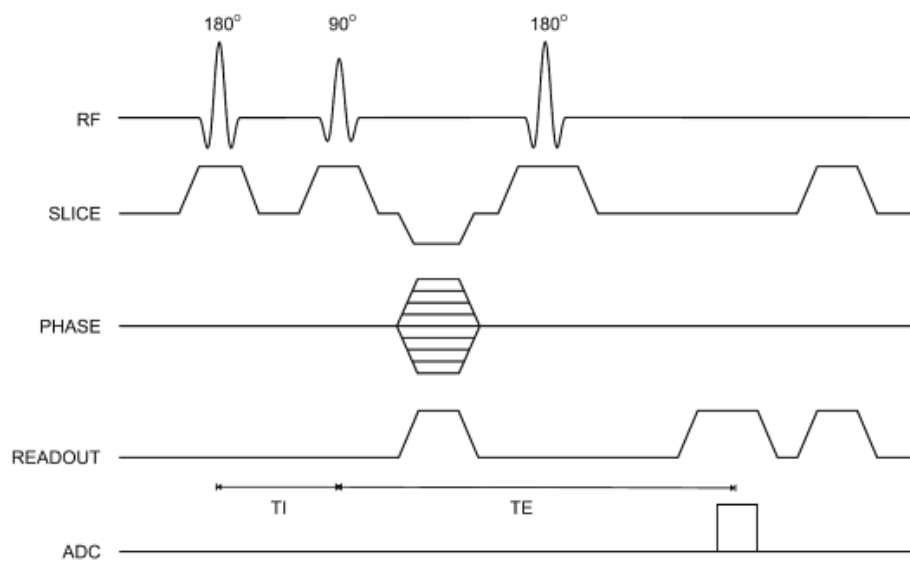


Figure 7: Inversion recovery pulse sequence timing diagram [49].

iii. Carr-Purcell-Meiboom-Gill pulse sequence (CPMG)

CPMG pulse sequence is commonly used pulse sequence to measure  $T_2$  relaxation times. In this sequence,  $90^\circ$  RF pulse is applied, followed by an echo train (series of  $180^\circ$  RF rephrasing pulses and their corresponding echoes) induced by successive  $180^\circ$  pulses as shown in Figure 8.

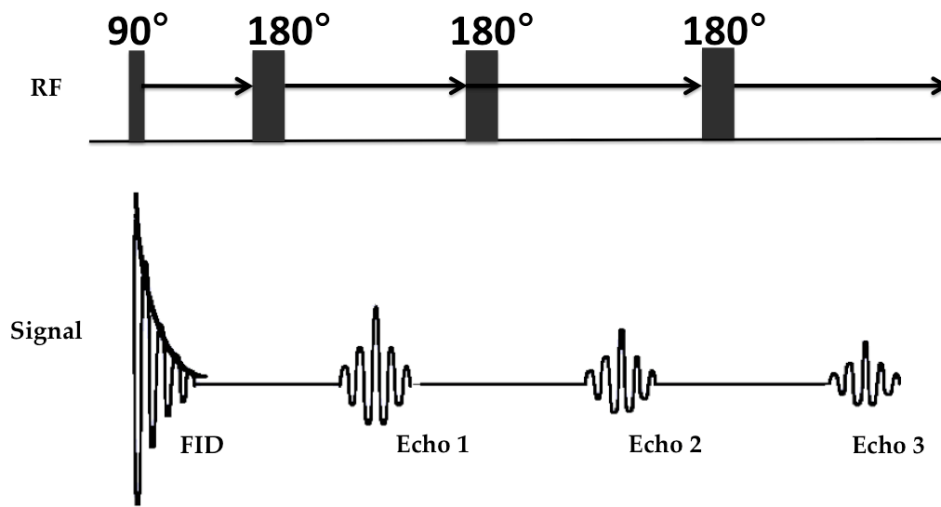


Figure 8: CPMG pulse sequence timing diagram [50].

iv. Multi slice Multi Echo Sequence (MSME)

Multi Slice Multi Echo (MSME) pulse sequence uses CPMG pulse sequence with slight variation. In CPMG pulse sequence,  $90^\circ$  RF pulse is applied, followed by successive  $180^\circ$  pulses with TE and acquisition periods as shown here.  $90^\circ$ -(TE/2)-(180°)-(TE/2)-(acq). In MSME, the same sequence is repeated for n times as  $(90^\circ)$ -

$(TE/2)-(180^\circ)-(TE/2)-(acq)$   $-(TE/2)-(180^\circ)-(TE/2)-(acq)-(TE/2)-(180^\circ)-(TE/2)-(acq)-\dots$  as illustrated in Figure 9 and this sequence produces n images.

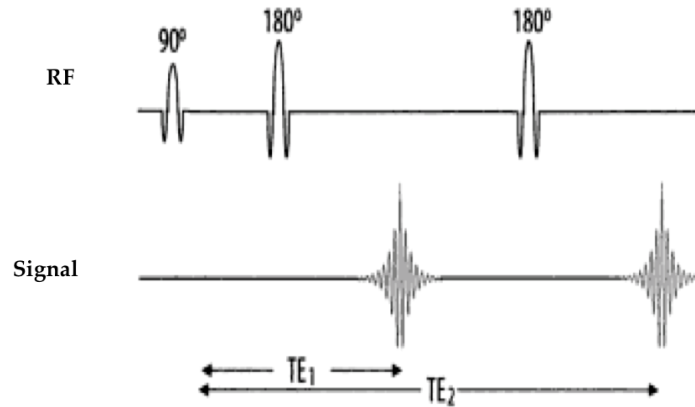


Figure 9: Multi slice multi echo sequence timing diagram [51].

v. Diffusion weighted spin echo pulse sequence

Diffusion weighted spin echo sequence is commonly used pulse sequence to measure ADC value. In this sequence,  $90^\circ$  RF pulse is applied, followed by two symmetrical gradient lobes placed on either side of the  $180^\circ$  refocusing pulse in a spin echo sequence (Figure 10). The strength of the applied gradient field and the square of the diffusion time during which the gradients are switched on are proportional to dephasing. Diffusion weighting becomes more feasible because of this sensitive gradient sequences and the use of high field gradient systems.

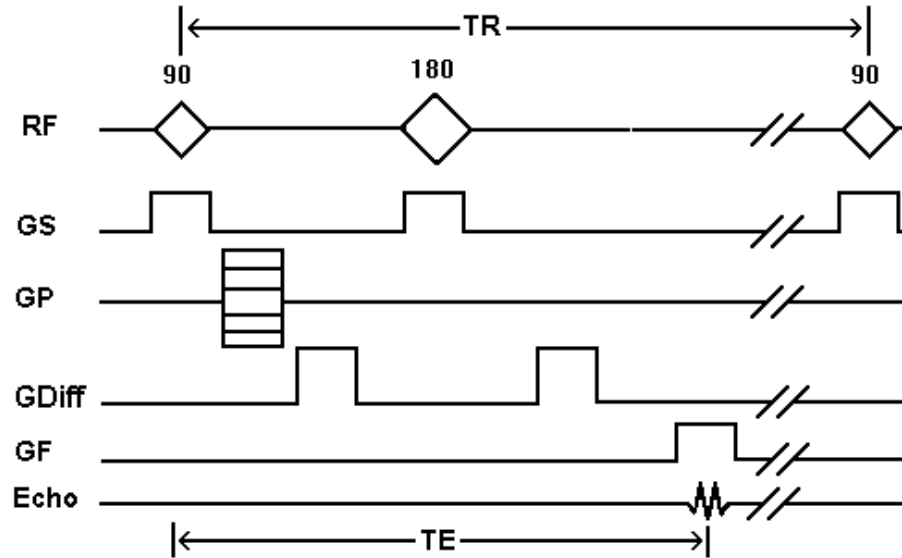


Figure 10: Diffusion weighted spin echo sequence timing diagram [52].

### 2.5.2. MRI Hardware

The MRI system consists of the following hardware components, which is shown in Figure 11.

- The most important and expensive component of MRI system is the main magnet. These magnets are of superconducting type and produce a static magnetic field  $B_0$ . The superconducting magnet is made of superconducting alloy (Nb/Ti) wire and is which is immersed in a liquid helium bath at 4.2K temperature. The coil and liquid Helium are placed in a can called Dewar, which is insulated by a vacuum jacket. The dewar is further cooled by liquid nitrogen at a temperature of 77.4K. When the sample is placed in this static

magnetic field  $B_0$ , the nuclei of the sample will be aligned to this magnetic field and generate a net magnetization  $M$  along  $Z$  direction.

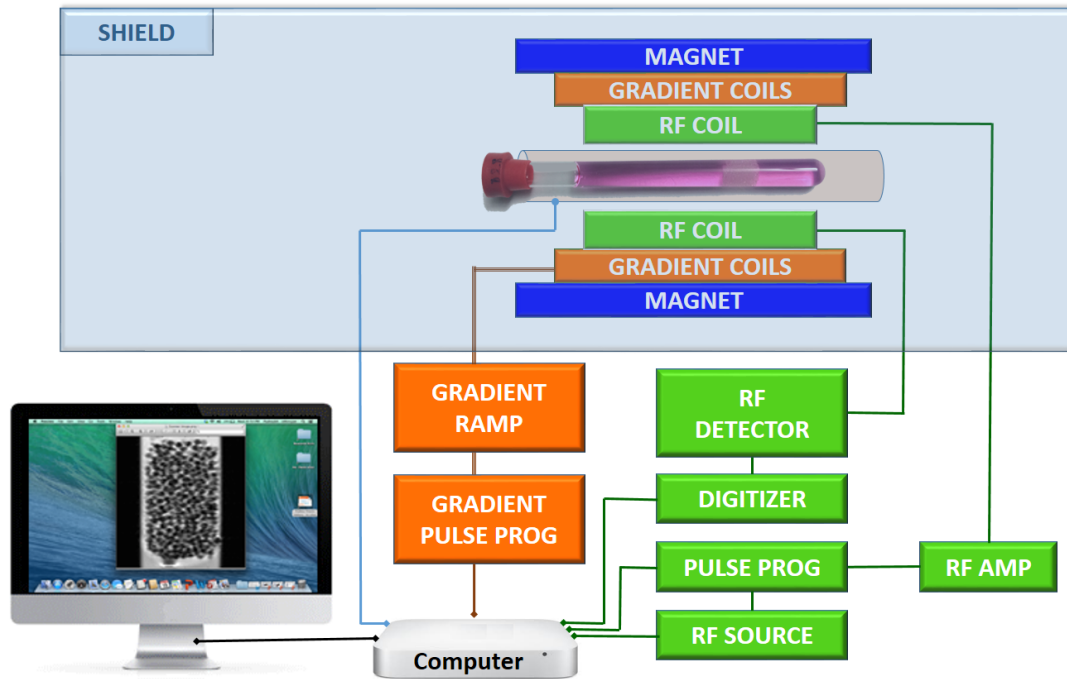


Figure 11: Schematic diagram of MRI scanner and components. This figure is inspired by [36].

- There are 3 different types RF coils; 1) transmit and receive coils that transmits RF energy to nuclei of the sample that make them excite from lower energy to a higher energy level. They also receives NMR signal from the imaged object and convert them into electric signals. 2) transmit only coils, and 3) receive only coils. RF coils can also be grouped into two different classes. Volume coils, which provides a homogeneous RF excitation across a large volume and surface

coils, which is specially designed for small area samples to provide a high RF sensitivity.

- The gradient system consists of three sets of coil in each direction. These coils are used to produce spatially varying gradients in the magnetic field,  $B_0$ . These gradient coils play the vital role in the image slice selections as well as frequency and phase encoding.

### 2.5.3. Sodium MRI

Sodium is the second largest NMR active abundant nuclei found in human body. Sodium plays an important role in physiology and cellular metabolism in human body; therefore sodium MRI is a subject of increasing interest [37]. Sodium MRI has the potential to provide complimentary information that is available from standard water  $^1\text{H}$  MRI. However, sodium MRI is a challenging technique due to the relatively low concentrations of sodium in biological tissues and low gyromagnetic ratio of sodium compared to protons. Many vital cellular functions depend on the maintenance of sodium concentration gradient. Healthy cells always maintain this concentration gradient while the impaired cell function leads to shift in this concentration gradient. Therefore, sodium is used as a biomarker for cancerous tissue. Sodium MRI is also used for quantification of sodium tissue for monitoring disease or the observing the tissue sodium in intracellular component.

### 3. MRI CHARACTERIZATION OF OSTEOGENIC AND CHONDROGENIC TISSUE CONSTRUCT

In this study, we characterized tissue-engineered bone and tissue-engineered cartilage using MRI. We performed T<sub>1</sub>, T<sub>2</sub> and ADC proton MRI experiments as well as sodium MRI experiments.

#### 3.1 Materials and Methods

##### 3.1.1. Sample Preparation

HMSCs (2 million/ml) were seeded in a matrix gel containing 1 mg/mL type I collagen and 1 mg/mL chitosan at 1:1 ratio. The osteogenic differentiation of HMSCs was directed with the aid of 100 µg/mL ascorbic acid, 10 mM β-glycerophosphate, and 10 mM dexamethasone in the differentiation media, whereas the chondrogenic differentiation was directed with the aid of 1% FBS, 1 mM dexamethasone, 50 mg/mL ascorbate-2 phosphate and 10 mg/ml TGF-β in αMEM differentiation media [6]. The samples were decellularized and kept in the refrigerator at -4 °C prior to MRI experiments. Figure 12 illustrates the schematic of sample preparation.

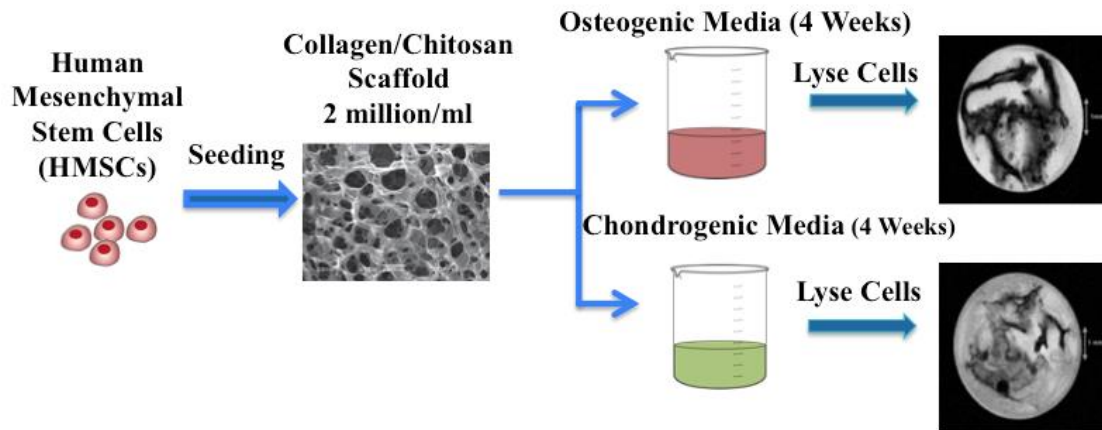


Figure 12: Schematic of chondrogenic and osteogenic construct preparation

### 3.1.2. Biochemical analysis

The figure 13 illustrates the confocal images of osteogenic and chondrogenic constructs stained for different ECM proteins. Fibronectin was used as positive control and tubulin served as negative control for the presence of intracellular protein. It is evident from the image that osteogenic proteins such as DMP1 were present in negligible quantities in the chondrogenic construct. Additionally, VEGF, the pro angiogenesis growth factor was absent in the chondrogenic construct. Cartilage being an avascular tissue necessitates that the chondrogenic constructs should not promote vascularization *in vivo*. Therefore, the absence of VEGF and reduced DMP1 indicated that the chondrogenic construct was anti osteogenic and pro chondrogenic in nature.

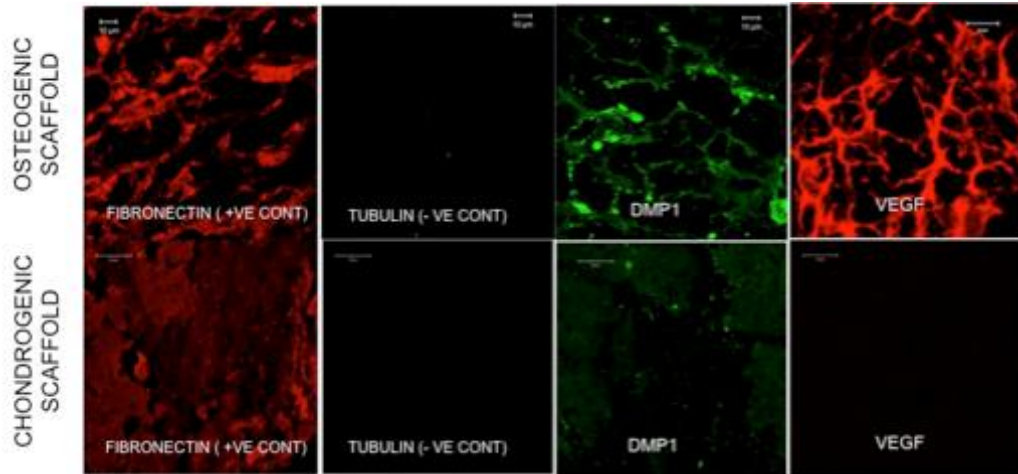


Figure 13: Confocal images of osteogenic and chondrogenic constructs stained for different ECM proteins.

### 3.1.3. Proton MRI measurements

The MRI measurements were performed using a Bruker 500 MHz (11.7 T) micro-imaging facility controlled by the Bruker imaging software Paravision 4.0 using a 5 mm proton RF coil (Figure 14). The samples were washed by HBSS (Hank's Balanced Salt Solution) and placed on top of 1% agarose gel in a 5 mm tube. Fluorinert oil was added for filling the RF coil volume. The  $T_2$  weighted image was acquired using a FLASH sequence [54]. The experimental parameters were: TE = 13ms, TR = 1000ms, FOV = 6 mm x 6 mm, matrix size = 128 x 128, slice thickness = 0.5 mm. The  $T_1$  parametric map was acquired using RAREVTR pulse sequence (RARE with variable TR) [55]. The experimental parameters were TE = 11.5 ms, TR (12 steps) = 114, 303, 512, 745, 1010, 1314, 1674, 2112, 2675, 3460, 4772, and 5500 ms, FOV = 6 mm x 6 mm, matrix size = 128 x 128, slice thickness = 0.5 mm. The  $T_2$  relaxation time measurements were

measured using MSME pulse sequence (multi slice multi echo) [51]. The experimental parameters were TE = 7.2 ms, TR = 4000 ms, FOV = 6 mm x 6 mm, matrix size = 128 x 128, slice thickness = 0.5 mm. The apparent diffusion coefficient (ADC) was obtained using diffusion weighted spin echo MRI sequence [52]. The experimental parameters were TE = 25.643ms, TR = 5000ms, b values (mm<sup>2</sup>/s) = 13, 213, 513, 813, 1213, 1613, FOV = 6 mm x 6 mm, matrix size = 128 x 128, slice thickness = 0.5 mm. The T<sub>1</sub>, T<sub>2</sub> and ADC maps were calculated by fitting voxel-by-voxel signal intensity to the single exponential fitting curve using a custom written Matlab program. The average value was derived from ROI of sample area.



Figure 14: (a) Bruker 500 MHz (11.7 T) micro-imaging facility, (b) Proton and proton/sodium double tuned 5mm RF coil.

### 3.1.4. Sodium MRI measurements

The  $^{23}\text{Na}$  MRI measurements were performed using a Bruker 500 MHz (11.7 T) micro-imaging facility controlled by the Bruker imaging software Paravision 4.0 using a 5 mm double tuned proton/sodium RF coil. The  $^{23}\text{Na}$  MRI images were acquired using the gradient echo with flow compensation (GEFC) pulse protocol. The experimental parameters were TE = 2 ms, TR = 100ms, FOV = 6 mm x 6 mm, matrix size = 128 x 128, slice thickness = 0.5 mm. The sodium concentration was calculated by using PBS ( $^{23}\text{Na}$  conc. = 154 mM) as a reference.

## 3.2 Results and Discussions

### 3.2.1. Proton MRI experiment

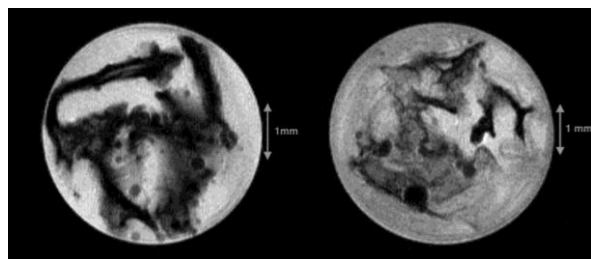


Figure 15: Axial slices from  $T_2$  weighted MRI images of osteogenic scaffolds (left) and chondrogenic scaffolds (right)

We acquired  $T_1$ ,  $T_2$  and ADC maps for osteogenic and chondrogenic constructs along with control collagen/chitosan gel. Figure 16 shows  $T_1$ ,  $T_2$  and ADC maps for

chondrogenic construct, osteogenic construct and the control along with the region of interest (ROIs) used for parameter calculation. Table 2 gives the calculated  $T_1$ ,  $T_2$  and ADC values for these samples along with their standard deviation. From the table, it is clear that there is no significant difference in the  $T_1$  values of both osteogenic and chondrogenic constructs. However, the  $T_2$  is found to be lower for osteogenic constructs when compared to chondrogenic constructs and both these values are lower than the gel  $T_2$ . It is interesting to note that the  $T_2/T_1$  ratio of osteogenic constructs is smaller as compared to the chondrogenic constructs. The values are: Osteo:  $T_2/T_1 = 0.025$ , Chondro:  $T_2/T_1 = 0.044$ . Also from the  $T_2$  weighted proton MRI images of osteogenic and chondrogenic constructs (shown in Figure 15) we can notice a clear difference in these constructs. The  $T_2$  weighted MRI image of osteogenic constructs is much darker as compared to chondrogenic constructs because of the shorter  $T_2$  for osteogenic construct. It also shows dark spots that may be coming from the mineral deposits in these constructs.

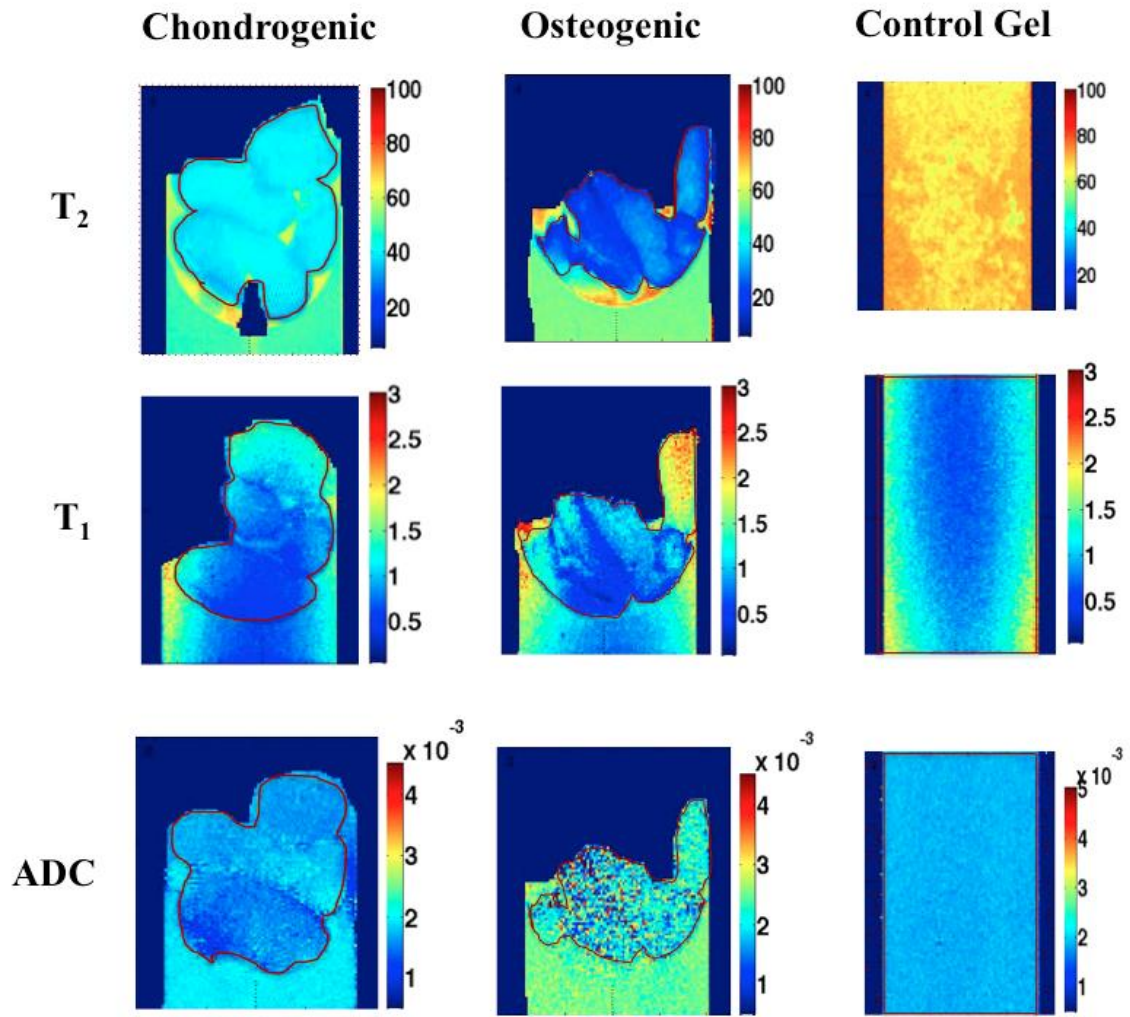


Figure 16: T<sub>1</sub>, T<sub>2</sub> and ADC maps of chondrogenic construct, osteogenic construct and control gel in Fluorinert oil.

Proton relaxation times for osteogenic and chondrogenic tissue constructs	Proton relaxation times (in Fluorinert oil)		
	T <sub>2</sub> (ms)	T <sub>1</sub> (s)	ADC 10 <sup>-3</sup> (mm <sup>2</sup> /s)
<b>Chondrogenic</b>	39.4 ± 1.9	0.89 ± 0.3	0.0016 ± 0.0002
<b>Osteogenic</b>	24.7 ± 3.6	0.97 ± 0.5	0.0019 ± 0.0006
<b>Collagen/Chitosan Gel</b>	67.4 ± 2.7	0.99 ± 0.3	0.0019 ± 0.0007

Table 3: Calculated mean and standard deviation of proton MRI parameters in collagen/chitosan gel, osteogenic and chondrogenic constructs

Apparent diffusion coefficient (ADC) is a well-known method, for measuring magnitude of water molecules mobility within the sample [38]. From the calculated value, we found that the ADC values were higher in the osteogenic construct than the to chondrogenic constructs. It is noted from the maps that chondrogenic constructs are very homogeneous whereas the osteogenic construct shows mixture of very low and high ADC values. These low ADC spots may be due to mineral deposits in osteogenic constructs.

### 3.2.2. Sodium MRI experiment

Finally, we utilized sodium MRI for proteoglycans quantification. As the Proteoglycans are negatively charged macromolecules, it will bind with positive sodium ions. Hence sodium concentration in the chondrogenic samples is

proportional to the concentration of proteoglycans (PG) and this method can be potentially used for PG quantification in engineered cartilage tissues [39]. Figure 13 shows sodium MRI image acquired using the double tuned sodium/proton RF coil at 11.7 T MRI system. Table 4 shows the Calculated average sodium concentration for osteogenic and chondrogenic tissue constructs. From the calculated values, we noticed that higher sodium concentration in chondrogenic constructs as compared to osteogenic constructs because of high amount of proteoglycans in these constructs.

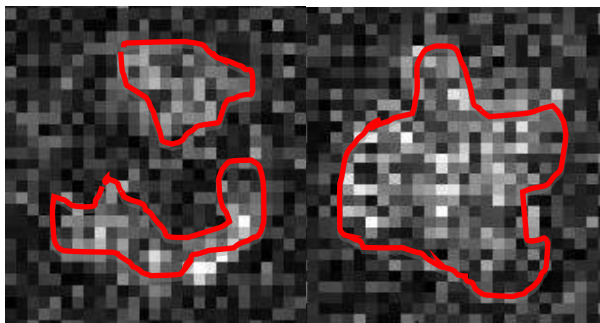


Figure 17: Image obtained from sodium MRI experiment at 11.7 T (left – osteogenic construct and right – chondrogenic construct)

	<b>Sodium Concentration</b>
<b>Chondrogenic construct</b>	189 mM $\pm$ 12 mM
<b>Osteogenic construct</b>	152 mM $\pm$ 20 mM

Table 4: Calculated average sodium concentration for osteogenic and chondrogenic constructs using sodium MRI

### 3.3 Conclusion

These results demonstrate the potential of multinuclear MRI in characterization of chondrogenic and osteogenic tissues. These techniques may be especially useful in preclinical and clinical studies for monitoring osteochondral interfaces that exhibit both bone and cartilage layers.

#### 4. MRI CHARACTERIZATION OF POLYMER - HYDROGEL SCAFFOLD, ECM, CELLS

Current MRI characterization technique for engineered cartilage tissues are based on correlation of water MR parameters, for example the relaxation times  $T_1$  or  $T_2$ , with extracellular matrix components, proteoglycans and collagen [7, 9]. This approach is based on such correlation of MR parameter with ECM in natural cartilage tissue [7]. However, engineered tissues have high amount of cells (stem cells and chondrocytes) and a biocompatible scaffold not found in natural tissues (show in Figure 3), therefore there is a need to develop new tools. Currently, MRI characterization of engineered cartilage ignores the interaction of water protons with cells that includes both intracellular and extracellular spaces, and biocompatible scaffolds. These are often the dominating contributions in water MR parameters of growing engineered tissues. In the current study, we present preliminary MRI data for chondrogenic differentiation of human bone marrow derived stem cells seeded onto the specially designed “polymer-hydrogel” osteochondral matrices to separate out various contributions in water  $T_2$  relaxation time. The scaffold system used here is uniquely designed to best support osteochondral defect repair and regeneration. The MRI characterization of these chondrogenic scaffolds was performed for scaffold only, scaffold with cells and ECM, and acellular scaffold with ECM. We identified the contribution of ECM and cells in water  $T_2$ .

## 4.1 Materials and Methods

### 4.1.1. Scaffold Preparation

Stem cell differentiation is regulated by numerous cues in their microenvironment. The porous 3D tissue scaffold provides those cues and is the basis of tissue engineering. These scaffolds provide more physiological conditions to stem cells and allow for the development of discrete tissues [40, 41]. In tissue engineering, the most important thing is the design of a proper scaffold, which provides necessary biological and mechanical environment to the encapsulated cells. In order to yield functional native like cartilage tissues, 3D encapsulation of stem cells with hydrogels have been identified as excellent materials. These scaffolds are remodeled into tissue like structures by the deposition of ECM proteins produced by the cells within the scaffold. Hydrogels possessing high water content were used as biomaterials for tissue engineering because of their efficiency in transporting nutrients and waste products and unique biocompatibility [42].

In this project, we used hydrogel-based scaffold "Polymer-Hydrogel" with tuned gradient properties [43, 44]. Oil-in water emulsion of poly (85 lactide-co-15 glycolide) (PLGA) polymer solution was fabricated into microspheres. These PLGA microspheres were combined with increasing NaCl porogen from bottom to top using the thermal sintering and porogen leaching matrix fabrication method [39]. Then bone marrow derived human mesenchymal stem cells (BM-hMSCs) were combined with puramatrix hydrogel. This human bone marrow stromal cells (500 K/scaffold) embedded in the hydrogel were added to the pores of the gradient matrix and the cell-

seeded matrices were cultured in chondrogenic media for cellular differentiation and matrix formation [45]. The figure 18 illustrates the schematic diagram of the scaffold fabrication process. The scaffolds were 4 mm in diameter and 8 mm in height. For comparing the MRI parameters, we performed experiments in empty scaffold, scaffold on day 7, 19 and 26 with and without cells. These Acellular measurements were done by fixing the samples using formalin overnight. The next day samples were washed three times in culture medium before MRI measurements to remove any excess formalin.

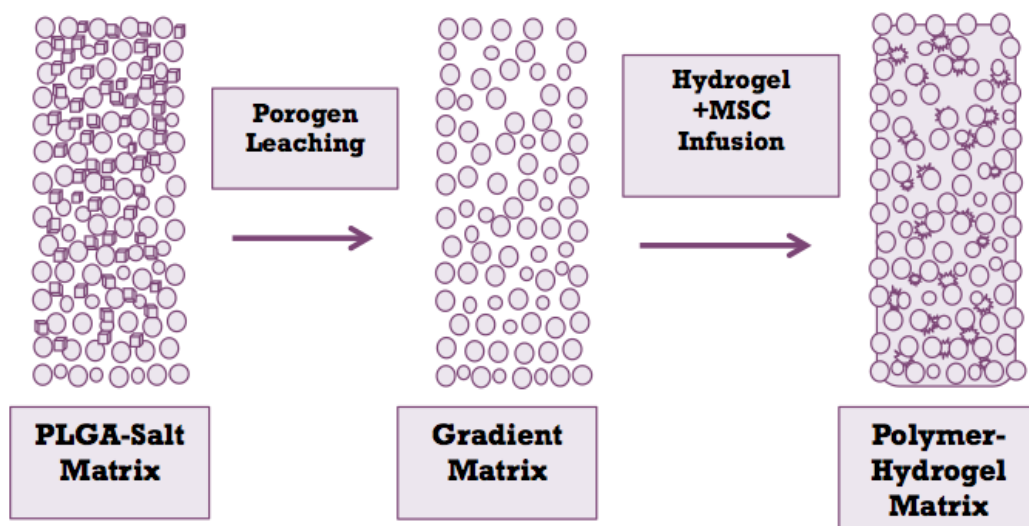


Figure 18: Schematic diagram of "Polymer-Hydrogel" scaffold fabrication

#### 4.1.2. Biochemical Analysis

Immunofluorescence staining was performed on the scaffold after 500,000 cells were seeded and cultured for 21 days is shown in Figure 19. From this biochemical analysis, the production of proteoglycans and collagen was confirmed.

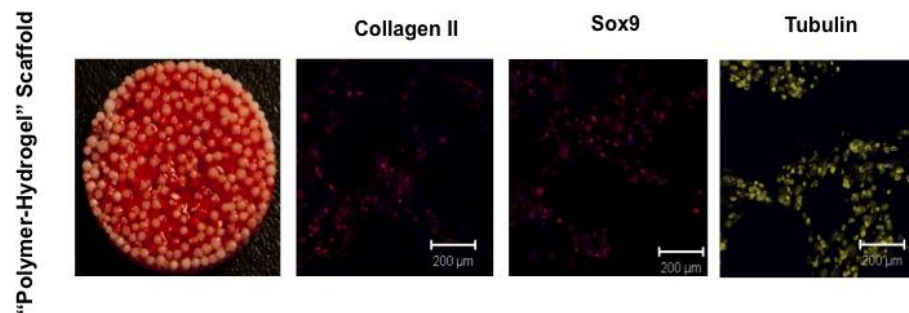


Figure 19: Immunofluorescence staining on the “Polymer Hydrogel “scaffold showing chondrogenesis of stem cells

#### 4.1.3. Proton MRI measurements

The MRI measurements were performed using a Bruker Avance DRX 11.7 T (500 MHz) micro-imaging facility controlled by the Bruker imaging software Paravision 4.0 using a 5 mm proton RF coil. The experiments were performed in chondrogenic growth media to preserve the natural environment of engineered tissues. The <sup>1</sup>H MRI experimental parameters were. The T<sub>1</sub> parametric map was acquired using RAREVTR pulse sequence (RARE with variable TR) [55]. The experimental parameters were TE = 11.447ms, TR (ms) = 113.8, 303.1, 511.9, 745.4, 1009.7, 1314.2, 1673.7, 2112.3, 2674.7, 3460.2, 4771.8, 5500 with 12 steps, FOV = 10 mm x 10 mm, matrix size = 128 x 128, slice

thickness = 0.5 mm, In-plane resolution = 0.078 mm x 0.078 mm, number of slices = 7. The T<sub>2</sub> relaxation time measurements were measured using MSME pulse sequence (multi slice multi echo) [51]. The experimental parameters were TE = 7.2ms, TR = 4000ms, FOV = 10 mm x 10 mm, matrix size = 128 x 128, slice thickness = 0.5 mm, In-plane resolution = 0.078 mm x 0.078 mm, number of slices = 7. The apparent diffusion coefficient (ADC) was obtained using diffusion weighted spin echo MRI sequence [52]. The experimental parameters were TE = 25.6 ms, TR = 5000 ms, b-values (s/mm<sup>2</sup>) = 13.3, 212.8, 512.8, 812.8, 1212, 1612, FOV = 10 mm x 10 mm, matrix size = 128 x 128, slice thickness = 0.5 mm, In-plane resolution = 0.078 mm x 0.078 mm, number of slices = 7.

#### 4.2 Results and Discussions

The various contributions in MR relaxation times and diffusion coefficients can be written as

$$\frac{1}{T_2(\text{cells, scaffold, ECM})} = \frac{1}{T_{2,\text{scaffold}}} + \frac{1}{T_{2,\text{cells}}} + \frac{1}{T_{2,\text{ECM}}} \quad (1)$$

The T<sub>2</sub> values for cells and ECM were calculated using the above equation 1 [47]. Table 1 presents the measured T<sub>2</sub> values in first three columns and calculated T<sub>2</sub> values for cells and ECM independently as highlighted boxed for Day 7, 19 and 26. Figure 20 shows the T<sub>2</sub> maps of these scaffolds with and without cells at day 7 and day 26 along with empty scaffold. Table 5 presents T<sub>1</sub> and ADC values for scaffolds on Day 7, 19 and 26 along

with empty scaffold.

Polymer Hydrogel Scaffold with HMSCs	T <sub>2</sub> (Cells +ECM+ Scaffold) (ms)	T <sub>2</sub> (ECM+ Scaffold) (ms)	T <sub>2</sub> (Scaffold) (ms)	T <sub>2</sub> (ECM) (ms)	T <sub>2</sub> (Cells) (ms)
Day 7	88.04 (±0.2) [B]	89.64 (±0.21) [D]	96.88 (±0.34) [A]	1251.8	894.2
Day 19	89.33 (±0.31)	101.91 (±0.57)	96.88 (±0.34) [A]	880.9	608.6
Day 26	90.1 (±0.32) [C]	113.7 (0.46) [E]	96.88 (±0.34) [A]	1016.2	619.8

Table 5: Measured and calculated T<sub>2</sub> for the scaffold system with and without cells, T<sub>2</sub> for ECM growth only and T<sub>2</sub> for cells at day 7,19 and 26.

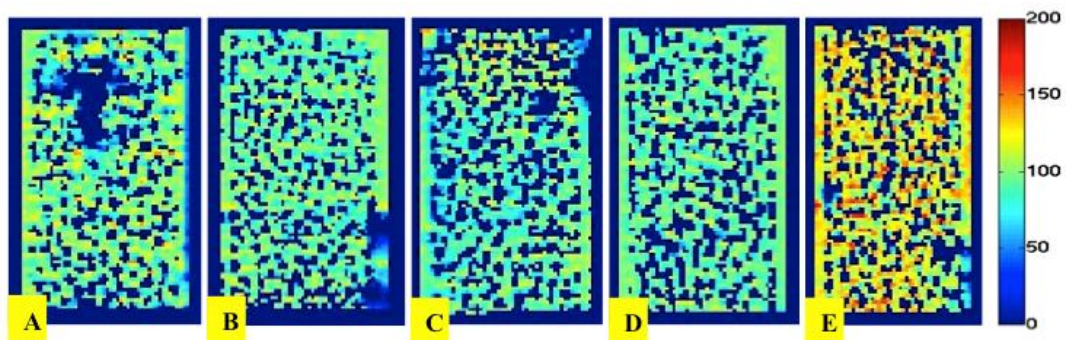


Figure 20: T<sub>2</sub> maps for (A) scaffold (B) engineered cartilage (scaffold + cells + ECM) at day 7 (C) engineered cartilage at day 26 (D) engineered cartilage-without-cells (ECM + scaffold) at day 7 (E) engineered cartilage-without-cells at day 26. The color bar is in ms.

It is clear from the table that the contribution of water-scaffold interaction in  $T_2$  is the most dominating contribution for these engineered tissues. It would hinder the observation of growing ECM and proliferating and differentiating BM-hMSCs in chondrocytes if not accounted for.

<b>Polymer Hydrogel Scaffold with HMSCs</b>	<b><math>T_1</math> (Cells +ECM+ Scaffold) (s)</b>	<b><math>T_1</math> (ECM+ Scaffold) (s)</b>	<b><math>T_1</math> (Scaffold) (s)</b>	<b>ADC (Cells +ECM+ Scaffold) (<math>10^{-3}</math> mm<sup>2</sup>/s)</b>	<b>ADC (ECM+ Scaffold) (<math>10^{-3}</math> mm<sup>2</sup>/s)</b>	<b>ADC (Scaffold) (<math>10^{-3}</math> mm<sup>2</sup>/s)</b>
<b>Day 7</b>	3.59 ( $\pm 0.005$ )	3.62 ( $\pm 0.004$ )	3.39 ( $\pm 0.006$ )	2.46 ( $\pm 0.002$ )	2.57 ( $\pm 0.001$ )	2.54 ( $\pm 0.001$ )
<b>Day 19</b>	3.26 ( $\pm 0.007$ )	3.76 ( $\pm 0.005$ )	3.39 ( $\pm 0.006$ )	2.49 ( $\pm 0.001$ )	2.51 ( $\pm 0.002$ )	2.54 ( $\pm 0.001$ )
<b>Day 26</b>	3.23 ( $\pm 0.007$ )	3.37 (0.007)	3.39 ( $\pm 0.006$ )	2.51 ( $\pm 0.001$ )	2.47 ( $\pm 0.001$ )	2.54 ( $\pm 0.001$ )

Table 6: Measured  $T_1$  and ADC for the scaffold system with and without cells at day 7, 19 and 26.

#### 4.3 Conclusions

This study shows that MR parametric imaging is sensitive to changes in scaffold properties, cell densities and ECM growth in growing engineered cartilage. We show that the contribution of scaffold and cells are non-negligible in water MR parameters. This contribution should be accounted for non-invasive MRI quantification of tissue growth for engineered tissues.  $T_2$  maps were found to be more sensitive to these contributions.

## 5. CONCLUSIONS AND FUTURE WORK

From these studies, we can demonstrate the potential of multinuclear MRI in characterization of chondrogenic and osteogenic tissues. These techniques may be especially useful for osteochondral constructs which exhibit both bone and cartilage layers and can be used in preclinical and clinical studies. Hence we conclude that MRI is a powerful and sensitive tool to assess growing osteochondral tissue regeneration. Further work is underway to apply these techniques for non-invasive monitoring of osteochondral graft *in vitro* and *in vivo* in animal models.

## 6. REFERENCES

- [1] "Prevalence and most common causes of disability among adults--United States, 2005", MMWR Morb Mortal Wkly Rep, 2009, 58, (16): 421-426.
- [2] Clair, B.L., A.R. Johnson, and T. Howard. "Cartilage repair: current and emerging options in treatment". Foot Ankle Spec, 2009. 2(4): 179-88.
- [3] Ahmed TAE, Hincke MT. "Strategies for articular cartilage lesion repair and functional restoration". Tissue Eng. Part B Rev. 2010; 16(3): 305–329.
- [4] Mithoefer, K., K. Hambly, S. Della Villa, H. Silvers and B. R. Mandelbaum (2009). "Return to sports participation after articular cartilage repair in the knee: scientific evidence." Am J Sports Med 37 Suppl 1: 167S-176S.
- [5] Duchow J, Hess T, Kohn D. "Primary stability of press-fit-implanted osteochondral grafts". Am. J. Sports Med. 2000; 28(1): 24–27.
- [6] Ravindran, S., Q. Gao, M. Kotecha, R. L. Magin, S. Karol, A. Bedran-Russo and A. George (2012). "Biomimetic extracellular matrix-incorporated scaffold induces osteogenic gene expression in human marrow stromal cells." Tissue Eng. Part A **18**(3-4): 295-309.
- [7] M. Kotecha, D. Klatt, and R.L. Magin (2013). "Monitoring cartilage tissue engineering using magnetic resonance spectroscopy, imaging, and elastography", Tissue Eng. Part B, Reviews, 19, (6): 470-484.
- [8] Kotecha M, Ravindran S, Vaidyanathan A, George A, Magin RL. "Characterization of ECM embedded biomimetic scaffolds for cartilage tissue engineering using sodium

- triple quantum coherence spectroscopy". Proceedings of the International Society for Magnetic Resonance in Medicine (ISMRM).
- [9] Kotecha, M., S. Ravindran, T. M. Schmid, A. Vaidyanathan, A. George and R. L. Magin (2013). "Application of sodium triple-quantum coherence NMR spectroscopy for the study of growth dynamics in cartilage tissue engineering." *NMR Biomed* **26**(6): 709-717.
- [10] Ling, W., R. R. Regatte, M. E. Schweitzer and A. Jerschow (2008). "Characterization of bovine patellar cartilage by NMR." *NMR Biomed* **21**(3): 289-295.
- [11] Lanza R. P., Langer, Robert S., Vacanti J. "Principles of tissue engineering 4<sup>th</sup> Edition". Academic Press; 2013
- [12] Ikada, Yoshito. "Tissue Engineering: Fundamentals And Applications". Amsterdam: Academic Press/Elsevier, 2006. Print.
- [13] <http://www.bioeng.nus.edu.sg/research/keyresearch/keysrh1.html>
- [14] Carney, B. J. and K. Shah (2011). "Migration and fate of therapeutic stem cells in different brain disease models." *Neuroscience* **197**: 37-47.
- [15] Pavlovic M., Bálint B. "Stem cells and tissue engineering". New York: Springer (2013).
- [16] Flanagan, T. C. and A. Pandit (2003). "Living artificial heart valve alternatives: a review." *Eur Cell Mater* **6**: 28-45; discussion 45.
- [17] Rita A. Deprich (2009). "Biomolecule Use in Tissue Engineering". *Fundamentals of Tissue Engineering and Regenerative Medicine*: 121-135
- [18] Marolt, D., M. Knezevic and G. V. Novakovic (2010). "Bone tissue engineering with human stem cells." *Stem Cell Res Ther* **1**(2): 10.

- [19] Pei, M., J. T. Li, M. Shoukry and Y. Zhang (2011). "A review of decellularized stem cell matrix: a novel cell expansion system for cartilage tissue engineering." *Eur Cell Mater* **22**: 333-343; discussion 343.
- [20] P. Pothirajan, D. Dorcemus, S. Nukavarapu, M. Kotecha. "True MRI Assessment of Stem Cell Chondrogenesis in a Tissue Engineered Matrix" at 36th Annual International Conference of the IEEE Engineering in Medicine and Biology Society-EMBC'14 at Chicago, IL
- [21] Pearle, A. D., R. F. Warren and S. A. Rodeo (2005). "Basic science of articular cartilage and osteoarthritis." *Clin Sports Med* **24**(1): 1-12.
- [22] Egli, P. S., E. B. Hunziker and R. K. Schenk (1988). "Quantitation of structural features characterizing weight- and less-weight-bearing regions in articular cartilage: a stereological analysis of medial femoral condyles in young adult rabbits." *Anat Rec* **222**(3): 217-227.
- [23] Meachim G, Sheffield SR. (1969). "Surface ultrastructure of mature adult human articular cartilage". *J Bone Joint Surg Br*: 51.
- [24] Stockwell RA (1971). "The interrelationship of cell density and cartilage thickness in mammalian articular cartilage". *J Anat* : 411-421
- [25] Muir H, Bullough P, Maroudas A (1970). "The distribution of collagen in human articular cartilage with some of its physiological implications". *J Bone Joint Surg Br*: 52
- [26] Hunziker EB, Michel M, Studer D. "Ultrastructure of adult human articular cartilage matrix after cryotechnical processing". *Microsc Res Tech* 1997: 37

- [27] Venn M, Maroudas A. "Chemical composition and swelling of normal and osteoarthrotic femoral-head cartilage." *Ann Rheum Dis* 1977: 36.
- [28] Radin EL, Rose RM (1986). "Role of subchondral bone in the initiation and progression of cartilage damage". *Clin Orthop Relat Res*; (213): 34–40.
- [29] Madry H, van Dijk CN, Mueller-Gerbl M (2010). "The basic science of the subchondral bone". *Knee Surg Sports Traumatol Arthrosc*: 18
- [30] Xu H, Othman SF, Hong L, Peptan IA, Magin RL (2006). "Magnetic Resonance Microscopy For Monitoring Osteogenesis In Tissue-Engineered Construct *In Vitro*". *Physics In Medicine And Biology*; 51(3): 719–732
- [31] Liang ZP, Lauterbur PC. "Principles Of Magnetic Resonance Imaging: A Signal Processing Perspective". New York, IEEE Press; 2000
- [32] F. Bloch, "Nuclear Induction," *Phys.Rev.*, 70:460-474; 1946.
- [33] Hashemi RH and Bradley WG Jr. "MRI: The Basics". Williams & Williams, Baltimore, MD, 1997.
- [34] Neil E. Jacobsen. "NMR Spectroscopy Explained: Simplified Theory, Applications and Examples for Organic Chemistry and Structural Biology". John Wiley & Sons, Sep 10, 2007
- [35] Conolly, S., G. Glover, D. Nishimura and A. Macovski (1991). "A reduced power selective adiabatic spin-echo pulse sequence." *Magn Reson Med* 18(1): 28-38.
- [36] [http://www.fas.org/irp/imint/docs/rst/Intro/Part2\\_26c.html](http://www.fas.org/irp/imint/docs/rst/Intro/Part2_26c.html)
- [37] [http://www.mri.jhmi.edu/~rouwerke/rouwerke\\_data/JACR4p741.pdf](http://www.mri.jhmi.edu/~rouwerke/rouwerke_data/JACR4p741.pdf)

- [38] D Chien, K K Kwong, D R Gress, F S Buonanno, R B Buxton, and B R Rosen (1992). "MR diffusion imaging of cerebral infarction in humans". *AJNR Am J Neuroradiol* 13: 1097-102
- [39] Yu D, Yin Z, Kotecha M. "Quantification of Proteoglycans in Tissue Engineered Cartilage using Sodium Imaging at 11.7T". *BMES-midwest career fair*; April 19<sup>th</sup>, 2013.
- [40] Hwang, N. S., M. S. Kim, S. Sampattavanich, J. H. Baek, Z. Zhang and J. Elisseeff (2006). "Effects of three-dimensional culture and growth factors on the chondrogenic differentiation of murine embryonic stem cells." *Stem Cells* **24**(2): 284-291.
- [41] N.S. Hwang, S. Varghese, and J. Elisseeff. "Cartilage tissue engineering: Directed differentiation of embryonic stem cells in three-dimensional hydrogel culture". *Methods Mol Biol*, 2007, 407, pp. 351-373.
- [42] Dorcemus D.L., Nukavarapu S.P. "Novel and Unique Matrix Design for Osteochondral Tissue Engineering". *Proc. 2013 MRS Fall meeting, Materials Research Society, Boston, MA, Dec 1-6 2013*.
- [43] Igwe J.C., Mikael P.E., Nukavarapu S.P. "Design, fabrication and in vitro evaluation of a novel polymer-hydrogel hybrid scaffold for bone tissue engineering". *J Tissue Eng. Regen. Med.* 2014 Feb;8(2): 131-42.
- [44] Dorcemus D.L., Nukavarapu S.P. "Osteochondral tissue engineering: Current strategies and challenges". *Biotechnology Advances*; 2013; 31; 5; pages 706-721.
- [45] Amini A.R., Laurencin C.T., Nukavarapu S.P (2012). "Bone Tissue Engineering: Recent advances and challenges". *Tissue Eng Part A* 18

- [46] Dorcemus D.L., Nukavarapu S.P. "Novel and unique matrix design for osteochondral tissue engineering". MRS proceedings; in press.
- [47] Fieremans E., Novikov D.S., Jensen J.H, Helpert J.A. "Monte Carlo study of a two-compartment exchange model of diffusion". NMR Biomed. Aug 2010; 23(7): 711-724;
- [48] Anne S., Fabiana D. S. A., Petra P., Therese A. "Metabolic alterations associated with schizophrenia: a critical evaluation of proton magnetic resonance spectroscopy studies". Journal of Neurochemistry; 2014; 128; pages 1-87.
- [49] Havla, L., T. Basha, H. Rayatzadeh, J. L. Shaw, W. J. Manning, S. B. Reeder, S. Kozerke and R. Nezafat (2013). "Improved fat water separation with water selective inversion pulse for inversion recovery imaging in cardiac MRI." J Magn Reson Imaging 37(2): 484-490.
- [50] Yamada S, Matsuzawa T, Yamada K, Yoshioka S, Ono S, Hishinuma T. "A modified signal intensity equation of Carr-Purcell-Meiboom-Gill pulse sequence for MR imaging." Tohoku J Exp Med 158(3) (July 1989): 203-209.
- [51] Serai, Suraj Dilip. "MRI Studies of In-vitro Perfused Pancreatic Islet Cell Activation: Correlation with Studies of Rat Models". PhD Thesis, Chicago: ProQuest, 2008.
- [52] R D Tien, G J Felsberg, H Friedman, M Brown, and J MacFall. "MR imaging of high-grade cerebral gliomas: value of diffusion-weighted echoplanar pulse sequences." American Journal of Roentgenology, 1994: 671-677.
- [53] Harley, G. Lorna. "In vivo and in vitro applications of collagen-GAG scaffolds". Chemical Engineering Journal vol. 137 issue 1 March 15, 2008. p. 102-121.

- [54] J Fujinaga, Y., H. Yoshioka, T. Sakai, Y. Sakai, F. Souza and P. Lang (2014). "Quantitative measurement of femoral condyle cartilage in the knee by MRI: Validation study by multireaders." *J Magn Reson Imaging* 39(4): 972-977.
- [55] Karfeld-Sulzer, L. S., E. A. Waters, E. K. Kohlmeir, H. Kissler, X. Zhang, D. B. Kaufman, A. E. Barron and T. J. Meade (2011). "Protein polymer MRI contrast agents: Longitudinal analysis of biomaterials in vivo." *Magn Reson Med* 65(1): 220-228.

## 7. VITA

PADMABHARATHI POTHIRAJAN

### Education

- Master of Science in Bioengineering Aug 2012 - May 2014  
University of Illinois at Chicago  
Thesis title: "Magnetic resonance characterization of stem cell based tissue - engineered cartilage and bone"
- Bachelor of Engineering in Electronics and Instrumentation Aug 2004 - May 2008  
Anna University, India

### Research Experience

- Department of Bioengineering, University of Illinois at Chicago, IL Jan 2013 - May 2014  
Magnetic Resonance quantification of tissue engineered bone, cartilage and Polymer-Hydrogel Scaffold
- Cellular Biosensor Lab, University of Utah at Salt Lake City, UT Dec 2010 - May 2011  
Applied electrophysiological techniques and time-lapse imaging to study calcium transients after pulsed IR in cardiomyocytes and neurons.
- Coromandel Electronics at Chennai, India Jan 2008 - May 2008  
Designed a model, "Patient Health Tracker using RFID tags" to help home patients that needed to be monitored closely for blood pressure, oxygen rate, and heart rate and especially for patients

### Conference Publication

- P. Pothirajan, D. Dorcemus, S. Nukavarapu, M. Kotecha; "True MRI Assessment of Stem Cell Chondrogenesis in a Tissue Engineered Matrix" submitted for presentation at 36th Annual International Conference of the IEEE Engineering in Medicine and Biology Society-EMBC'14 at Chicago, IL, Aug 26-30, 2014.
- P. Pothirajan, S. Ravindran, A. George, R. Magin, and M. Kotecha; "Magnetic Resonance Spectroscopy and Imaging Can Differentiate between Engineered Bone and Engineered Cartilage" submitted for presentation at 36th Annual International Conference of the IEEE Engineering in Medicine and Biology Society-EMBC'14 at Chicago, IL, Aug 26-30, 2014.
- P. Pothirajan, D. Dorcemus, S. Nukavarapu, M. Kotecha; "Identifying Contributions from Scaffolds, Cells and Extracellular Matrix in MRI of Polymer-Hydrogel-based Engineered Cartilage" at 2014 Annual Meeting and Exposition- Society For Biomaterials at Denver, CO, Apr 16-19, 2014.
- P. Pothirajan, R. Magin, M. Kotecha; "Magnetic resonance characterization of ECM integrated scaffolds for bone and cartilage tissue engineering" at 2013 BMES Annual Meeting at Seattle, WA, Sept 25-28, 2013.
- P. Pothirajan, D. Dorcemus, S. Nukavarapu, M. Kotecha; "Standardization of parametric MRI quantification of stem cell-based tissue-engineered cartilage" at Stem Cell and Regenerative Medicine Symposium at UIC, Chicago, IL, Sept 20, 2013.
- P. Pothirajan, R. Magin, M. Kotecha; "Characterization of engineered cartilage and bone using Magnetic Resonance Spectroscopy" at 2013 BMES Midwest Conference at Chicago, IL, Apr 19, 2013.